Shape instabilities in confined ferrofluids under crossed magnetic fields

Rafael M. Oliveira,[1,*] Írio M. Coutinho,[2,†] Pedro H. A. Anjos,[3,‡] and José A. Miranda[2,§]
[1]*Departamento de Engenharia Mecânica, Pontifícia Universidade Católica do Rio de Janeiro, Rio de Janeiro, 22451-900 Brazil*
[2]*Departamento de Física, Universidade Federal de Pernambuco, Recife, Pernambuco 50670-901 Brazil*
[3]*Department of Applied Mathematics, Illinois Institute of Technology, Chicago, Illinois 60616, USA*

(Received 14 September 2021; accepted 16 December 2021; published 30 December 2021)

We analyze the morphology and dynamic behavior of the interface separating a ferrofluid and a nonmagnetic fluid in a Hele-Shaw cell, when crossed radial and azimuthal magnetic fields are applied. In addition to inducing the formation of a variety of eye-catching, complex interfacial structures, the action of the crossed fields makes the deformed ferrofluid droplet to rotate. Numerical simulations and perturbative mode-coupling theory are employed to look into early linear, intermediate weakly nonlinear, and fully nonlinear dynamic regimes of the pattern-forming process. We investigate how the system responds to variations in the viscosity difference between the fluids, the magnetic susceptibility of the ferrofluid, the effects of surface tension, and in the relative strength between radial and azimuthal applied magnetic fields. The role played by random perturbations at the initial conditions in determining the ultimate shape and dynamic stability of the spinning ferrofluid patterns is also studied.

DOI: 10.1103/PhysRevE.104.065113

I. INTRODUCTION

Ferrofluids are stable colloidal suspensions of nanometer-sized magnetic particles suspended in a nonmagnetic carrier fluid. This magnetic fluid behaves superparamagnetically and can easily be manipulated with external magnetic fields [1,2]. The convenient combination of the fluidity of liquids and the magnetic properties of solids makes ferrofluids ideal materials to study a variety of interfacial instabilities, and pattern formation processes [3–7].

A popular setup used to investigate the development of patterns in ferrofluids is the situation in which a magnetic fluid drop, surrounded by a nonmagnetic fluid, is confined between the two closely spaced glass plates of a Hele-Shaw cell [8–11]. One emblematic example of such confined flow problems in ferrohydrodynamics is the occurrence of the so-called labyrinthine instability [12–15]. It takes place when a ferrofluid droplet is trapped in the cell, and a perpendicular uniform magnetic field is applied normal to the cell's plates. This perpendicular magnetic field arrangement is generated by a pair of Helmholtz coils having electric currents flowing in the same direction, while the Hele-Shaw cell is located at the mid-distance between the coils. The interplay between destabilizing magnetic forces and stabilizing surface tension effects ultimately leads to the emergence of mazelike, multiply bifurcated structures, where a labyrinth-type pattern arises.

A similar Helmholtz coils configuration can produce a very different applied magnetic field, which is able to produce quite distinct ferrofluid patterns in Hele-Shaw cells. Simply by considering that the electric currents in the coils flow in opposite directions (a configuration commonly known as the anti-Helmholtz arrangement [16–21]), one generates a radially symmetric magnetic field which is coplanar to the cell's plates. This radial magnetic field is zero at the axis of symmetry of the coils and increases linearly with the radial distance. As a result, a destabilizing magnetic body force acts on the ferrofluid droplet pointing in the outward radial direction. The competition of magnetic and surface tension forces provokes the formation of starfishlike polygonal shapes having sharp finger tips [22–24].

Another magnetic field configuration that has been used to study pattern-forming ferrofluid structures in Hele-Shaw geometry is the azimuthal magnetic field produced by a current-carrying wire. In this setting, a long straight wire is placed normal to the cell plates, passing through its center, where a ferrofluid droplet is located. The azimuthal magnetic field acts on the ferrofluid and generates a net magnetic body force pointing radially inwards. This force attracts the ferrofluid droplet toward the wire [1,25]. Depending on the position of the ferrofluid with respect to the nonmagnetic fluid, such azimuthal magnetic field effects can either stabilize or destabilize the two-fluid interface. For example, if the ferrofluid is the inner fluid, surrounded by an outer nonmagnetic fluid, then the azimuthal magnetic field tends to stabilize interfacial disturbances [25,26]. On the other hand, if the ferrofluid is the outer fluid, while the inner fluid is nonmagnetic, then the two-fluid interface is unstable, and one observes the formation of patterns very distinct from those obtained under perpendicular or radial applied magnetic fields. Steady droplet shapes presenting flat-tip, penetrating ferrofluid fingers, separated by balloon-shaped structures of the nonmagnetic fluid [27] have been identified. More convoluted, time-evolving shapes have

*rmo@puc-rio.br
†iriomenezes@gmail.com
‡pamorimanjos@iit.edu
§jose.mirandant@ufpe.br

also be found, presenting multiple invading ferrofluid fingers, divided by equally complex structures of the nonmagnetic fluid [28].

Researchers have also examined ferrofluid pattern formation in Hele-Shaw cells, when two different applied magnetic fields act simultaneously. This particular setup differs from previous pattern-forming investigations in ferrofluids in an important aspect, since now the two major competing forces are both magnetic in nature. In Refs. [29–32] experiments considered the action of a uniform perpendicular magnetic field, supplemented by an AC rotating magnetic field. These experiments revealed that a confined ferrofluid droplet undergoes to a peculiar morphological transition evolving from labyrinthine shapes to spiral patterns or suddenly morphing into visually striking protozoanlike shapes. In addition, investigators have considered the simultaneous operation of an applied stabilizing azimuthal magnetic field, plus a destabilizing perpendicular field to gain control over the mode selection mechanism of the pattern-forming system [33]. By using linear stability analysis and numerical simulations they have shown that such crossed magnetic field configuration can be used to control the morphology and number of fingers of the resulting patterns. Furthermore, in Ref. [34] this field composition has been utilized to control the shape of the patterns, as well as the degree of mixing between a miscible inner ferrofluid, and an outer nonmagnetic fluid via magnetic means.

An interesting recent study considered a different crossed magnetic fields arrangement, namely the action of both radial and azimuthal applied magnetic fields on confined ferrofluid droplets in a Hele-Shaw cell [35]. They have conducted a second-order weakly nonlinear analysis and fully nonlinear simulations to find that the combination of these two magnetic fields can induce rotation of a ferrofluid droplet having a stable shape, with velocities predictable by the proposed theory.

As commented in Ref. [35] their study opened up the possibility of using the crossed magnetic field configuration for controlling active fluid suspensions via magnetic means. Potential applications in soft matter systems are magnetic manipulation of shape-programmable microswimmers, microrobots, and giant magnetoliposomes [36–39]. Moreover, crossed magnetic field techniques could also be utilized to probe mechanical and rheological properties of certain biological materials such as developing tissues [40] and living cells [41]. Another interesting possibility is to use these crossed magnetic field controlling tools in biomedical processes involving magnetically operated drug targeting and delivery [42]. These more practical and interdisciplinary examples of soft matter, biomedical, and fluid mechanical systems involving the interaction of magnetic and hydrodynamic effects support the academic relevance and possible practical usefulness of studies like the ones presented in Ref. [35], and in this work.

In the current investigation, we further explore the system examined in Ref. [35] by analyzing a myriad of nonlinear pattern forming structures. We find that the presence of random noise at the early interface can render unstable some nonlinear shapes that would otherwise be stable had the initial condition received a symmetrical wavy perturbation. We also consider situations when the ferrofluid droplet can be either more or less viscous than the external nonmagnetic fluid surrounding the magnetic droplet. When the ferrofluid is less viscous, the inclusion of a Saffman-Taylor instability contribution to magnetically driven effects can also make the interface unstable, and we identify a bifurcation point characterizing this transition to instability. Finally, we verify that a third-order mode coupling perturbative analysis can capture the essential nonlinear morphological features of the interface of some less deformed patterns calculated by the boundary integral method.

We close this section by discussing how our current paper differs from the work carried out in Ref. [35]. Despite the significance and usefulness of their work, in Ref. [35] the authors restricted their study for the case in which the system's viscosity contrast $A = -1$, and the ferrofluid's magnetic susceptibility $\chi = 1$. In this setting, they found that the ferrofluid droplet reached a steady state, performing a rotating motion with a prescribed angular velocity, without ever changing its shape. On the other hand, in this work we analyze how the dynamical behaviors and shapes of the ferrofluid patterns respond, if the controlling parameters A and χ are changed. This raises some interesting questions about the problem. For instance, if A and χ assume values different from those examined in Ref. [35], then would the rotating ferrofluid droplet still reach a steady state? Moreover, what would be the new shapes of the ferrofluid droplets under such more general circumstances? And yet how sensitive is the system to the presence of random perturbations in the initial conditions? Here we address these pertinent questions, and while doing it, find other possible dynamical responses (the occurrence of both steady and transient or ever changing states), and still unexplored droplet shapes for the rotating patterns. Finally, it is worth pointing out that our current study certainly impacts the potential uses and applications mentioned above [36–42]. After all, since depending on the values of A and χ, one can get either steady or ever growing states for the ferrofluid droplet, it is indeed very important to know the proper values of such parameters in order to get an increased control of such processes. For an optimized control, in principle one would want to use values of A and χ that lead to steady states in which the ferrofluid droplet rotates with constant angular velocity, while keeping its shape immutable. Our work offers useful insights about the selection of these proper values for A and χ.

II. NUMERICAL AND THEORETICAL APPROACHES

A. Vortex sheet and the boundary integral method

The flow configuration of the physical problem is illustrated in Fig. 1. It shows a Hele-Shaw cell of gap thickness b, containing an initially circular droplet of ferrofluid of radius R and viscosity η_1, surrounded by a nonmagnetic fluid of viscosity η_2. The fluids are incompressible and Newtonian, and the surface tension between them is denoted by σ. This ferrohydrodynamic system is under the action of two crossed magnetic fields that are constant in time: an azimuthal field generated by a current-carrying wire passing through the center of the cell [25–27] and a radial magnetic field produced by two coils in the anti-Helmholtz configuration [22–24].

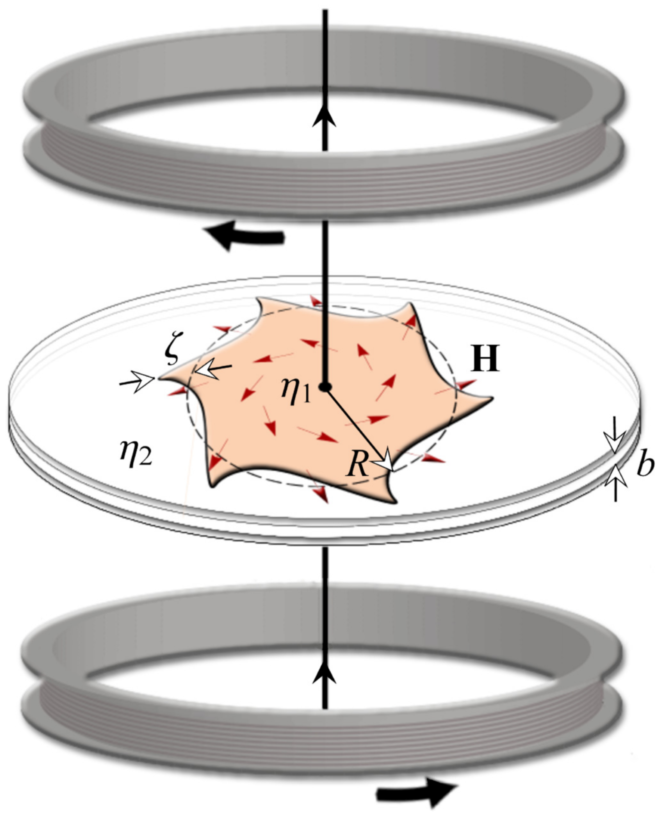

FIG. 1. Schematic representation of a ferrofluid droplet of viscosity η_1, surrounded by a nonmagnetic fluid of viscosity η_2, confined between the plates of a Hele-Shaw cell of gap thickness b. The system is subjected to a total magnetic field $\mathbf{H}$ which is a combination of radial and azimuthal magnetic fields [Eq. (2)]. The azimuthal magnetic field is produced by a long, straight current-carrying wire that is perpendicular to (coaxial with) the plates, while a radial magnetic field pointing outwards is generated by a pair of anti-Helmholtz coils having equal electric currents flowing in opposite directions. The Hele-Shaw cell is coaxial with, and parallel to, the coils and placed in the midplane between them. Initially, the ferrofluid droplet has a circular shape of radius R (dashed curve) but may deform due to the action of $\mathbf{H}$. Small interface perturbations are denoted by $\zeta = \zeta(\varphi, t)$, where φ is the azimuthal angle.

The fluids' displacements are described by Darcy's law, but the internal fluid has an augmented term to account for the magnetic contribution [12–14]

$$\mathbf{v}_j = -\frac{b^2}{12\eta_j}\nabla\left[p_j - \frac{1}{2}\mu_0\chi H^2\delta_{j1}\right], \tag{1}$$

where the applied magnetic field is given by

$$\mathbf{H} = \mathbf{H}_\varphi + \mathbf{H}_r = \frac{I}{2\pi r}\hat{\mathbf{e}}_\varphi + \frac{H_0}{R} r\hat{\mathbf{e}}_r. \tag{2}$$

The first (second) term on the right-hand side of Eq. (2) represents the applied azimuthal (radial) magnetic field, where $\hat{\mathbf{e}}_\varphi$ ($\hat{\mathbf{e}}_r$) is a unit vector in the azimuthal (radial) direction. Since the flow is incompressible, the velocity in the bulk of the fluids $j = 1$ and 2 is irrotational and given by $\mathbf{v}_j$, whereas p_j denotes the pressure, μ_0 is the magnetic permeability of free space, χ is the magnetic susceptibility of the ferrofluid, $H = |\mathbf{H}|$, and δ_{j1} is the Kronecker delta. In Eq. (2), the electric current generating the azimuthal field is given by I, while r measures the radial distance from the wire, and H_0 is the magnitude of the radial component at the initial droplet radius R.

To describe the evolution of the interface, we modify the boundary integral method previously employed in the calculation of nonlinear pattern formation of ferrofluid droplets subjected only to the radial magnetic field [24]. This method tracks the time evolution of the dimensionless vortex-sheet strength $\gamma = s_\alpha(\mathbf{v}_2 - \mathbf{v}_1)\cdot\hat{s}$, where $\hat{s}$ is the unit vector tangent to the two-fluid interface. The plane curve that describes this interface has the parameter α taken as the negative of the azimuthal angle and subscripts represent partial derivatives. After substituting Darcy's law from Eq. (1) and appropriate boundary conditions, as discussed below, the vortex-sheet yields

$$\begin{aligned}\gamma = &-2As_\alpha\mathbf{W}\cdot\hat{s} + 2B\frac{\theta_{\alpha\alpha}}{s_\alpha} - 2\chi\left(rr_\alpha - \chi r^3 r_\alpha\frac{\theta_\alpha}{s_\alpha^2}\right)\\ &+2\chi J^2\left\{\frac{r_\alpha}{r^3} - \chi\frac{r_\alpha}{r}\left[\frac{\theta_\alpha}{s_\alpha^2} - \frac{1}{s_\alpha^4}\left(\frac{r_\alpha^4}{r^2} - r^2\right)\right]\right\}\\ &+2\chi^2 J\left\{\frac{\theta_\alpha}{s_\alpha^2}(r_\alpha^2 - r^2) + \frac{1}{s_\alpha^4}(r_\alpha^4 - r^4)\right\},\end{aligned} \tag{3}$$

where lengths are rescaled by R, and velocities by $b^2\mu_0H_0^2/[12(\eta_1+\eta_2)R]$. Here s is the interface arclength, and θ denotes the tangent angle to the interface. Equation (3) is an integrodifferential equation that needs to be solved in every time step for the vortex sheet, γ, since the interface velocity, $\mathbf{W}$, is given by a Birkhoff-Rott integral that depends on γ [43–48]. By inspecting Eq. (3) one verifies that the system is characterized by four dimensionless governing parameters, namely,

$$A = \frac{\eta_2 - \eta_1}{\eta_2 + \eta_1}, \quad B = \frac{\sigma}{\mu_0 H_0^2 R}, \quad \chi, \quad J = \frac{I}{2\pi H_0 R}.$$

These parameters are the viscosity contrast A, the effective surface tension B, the magnetic susceptibility χ, and the dimensionless current J which measures the relative influence of azimuthal and radial magnetic fields. In deriving Eq. (3) we have employed a modified version of the Young-Laplace pressure jump boundary condition that includes contributions due to the interfacial surface tension, as well as to magnetic traction effects arising from the influence of the normal component of the ferrofluid's magnetization at the interface [1,2,24,49]

$$p_1 - p_2 = \sigma\kappa - \tfrac{1}{2}\mu_0(\mathbf{M}\cdot\hat{\mathbf{e}}_n)^2, \tag{4}$$

with $\mathbf{M} = \chi\mathbf{H}$, where $\mathbf{M}$ is the ferrofluid's magnetization. In Eq. (4), κ is the curvature of the fluid-fluid interface and $\hat{\mathbf{e}}_n$ indicates the unit normal vector to the interface. Notice that by setting $J = 0$ in Eq. (3) we recover the vortex sheet expression originally derived in Ref. [24] [their Eq. (4)], when the applied magnetic field has only the radial component. We point out that the terms inside the curly brackets multiplied by $2\chi^2 J$ in Eq. (3) originate from the coupling between the radial and azimuthal components. In fact, as discussed in the next section on the perturbative analysis, the coupling between these terms appear already at the linear stage.

Motivated by the Frenet-Serret expression, $\theta_\alpha = s_\alpha \kappa$, which simplifies the description of the plane curvature, time evolution of the nonlinear shapes of the interface employs as integration variables the Fourier transformed versions of the perimeter $L(t)$, and the tangent angle θ. To recover the coordinates of the interface, we calculate the complex position of the grid points through $z_\alpha = L/(2\pi)\exp(i\theta)$. Finally, we apply the small scale decomposition to reduce the stiffness of the governing equations. More details regarding the numerical implementation can be found in Refs. [24,45–48].

The validation of the numerical implementation was done reproducing linear stability results and through comparisons of the nonlinear numerical solutions with weakly nonlinear stages of the dynamics. This was conducted for the purely radial magnetic field, obtained by setting the dimensionless current $J = 0$, and presented in Sec. III and Figs. 1–3 of Ref. [24]. For the current investigation, additional validation tests were conducted. Some of them are discussed in Sec. IV, where a comparison between the current simulations and a third-order, perturbative analysis is examined.

B. Third-order, mode-coupling perturbative analysis

In this section, we develop a perturbative weakly nonlinear theory for the problem of an initially circular ferrofluid droplet subjected to crossed radial and azimuthal applied magnetic fields. In our perturbative analysis, the perturbed shape of the fluid-fluid boundary is described by $\mathcal{R}(\varphi, t) = R + \zeta(\varphi, t)$, where φ is the azimuthal angle. Here $\zeta(\varphi, t) = \sum_{n=-\infty}^{+\infty} \zeta_n(t) \exp(in\varphi)$ represents the net interface perturbation with complex Fourier amplitudes $\zeta_n(t)$, and integer azimuthal wave numbers n. Mass conservation imposes that the zeroth mode is written in terms of the other modes as $\zeta_0 = -(1/2R)\sum_{n=1}^{\infty}[|\zeta_n(t)|^2 + |\zeta_{-n}(t)|^2]$ [11].

Our perturbative approach will allow us to contrast some of the less deformed fully nonlinear shapes obtained by employing the boundary integral numerical method discussed in Sec. III, with corresponding interfacial patterns obtained by making use of a perturbative mode-coupling scheme. Therefore, here our leading goal is to find a differential equation which describes the time evolution of the perturbation amplitudes $\zeta_n(t)$, accurate to third-order [$O(\zeta_n^3)$]. The necessity of analyzing the problem perturbatively up to the third order is justified by the fact that the key morphological and dynamical effects can only be properly caught at such high orders. This will become very clear during the discussion of Sec. IV.

Recall that, as commented in Sec. II A, the flow is irrotational in the bulk. Consequently, we can state the problem in terms of a velocity potential, $\mathbf{v}_j = -\nabla\phi_j$ [1,2,8–14],

$$\phi_j = \sum_{n\neq 0} \phi_{jn}(t)\left(\frac{r}{R}\right)^{(-1)^{(j+1)}|n|} \exp(in\varphi), \tag{5}$$

which obeys Laplace's equation. Within this perturbative framing, we follow usual procedures adopted in previous weakly nonlinear studies in Hele-Shaw cells (see, for instance, Refs. [11,22,23]), consider $|\zeta| \ll R$, and use the kinematic boundary condition [8–10]

$$\frac{\partial \mathcal{R}}{\partial t} = \left[\frac{1}{r^2}\frac{\partial r}{\partial \varphi}\frac{\partial \phi_j}{\partial \varphi} - \frac{\partial \phi_j}{\partial r}\right]_{r=\mathcal{R}}, \tag{6}$$

to express the Fourier coefficients $\phi_{jn}(t)$ in terms of the perturbation amplitudes $\zeta_n(t)$, and their time derivatives $\dot{\zeta}_n(t) = d\zeta_n(t)/dt$. Next, we substitute the resulting relations, and the pressure jump condition [Eq. (4)] into Darcy's law [Eq. (1)]. Finally, by keeping terms consistently up to third-order in ζ, and Fourier transforming, we find the dimensionless equation of motion for the perturbation amplitudes $\zeta_n(t)$ (for $n \neq 0$)

$$\begin{aligned}\dot{\zeta}_n = {} & \lambda(n)\,\zeta_n + \sum_{p\neq 0}\{F(n,p) + \lambda(p)G(n,p)\}\,\zeta_p\zeta_{n-p} \\ & + \sum_{p,q\neq 0}\{[\lambda(p)I(n,p,q) + G(n,q)(F(q,p) \\ & + \lambda(p)G(q,p))]\,\zeta_p\zeta_{q-p}\zeta_{n-q} \\ & + [\mathcal{J}(n,p,q) + \lambda(p)K(n,p,q)]\,\zeta_p\zeta_q\zeta_{n-p-q}\}.\end{aligned} \tag{7}$$

In Eq. (7) the function

$$\lambda(n) = |n|[\chi(1+\chi) - \chi J^2 - B(n^2-1) - in\chi^2 J] \tag{8}$$

is a time-independent, complex linear growth rate. In Eq. (8), the first term inside the squared brackets represents a destabilizing effect related to the radial component of the magnetic field. In contrast, the second and third terms account for the stabilizing contributions coming from the azimuthal component of the magnetic field, and surface tension at the interface, respectively. The presence of an imaginary part in Eq. (8) is responsible for the propagation of the perturbed interfacial shape, with linear phase velocity given by $v(n) = -\mathrm{Im}[\lambda(n)]/n = \chi^2 J|n|$. After reintroduction of dimensions, one can readily verify that such velocity vanishes for a purely radial (i.e., $H_0 \neq 0$ and $I = 0$) or azimuthal (i.e., $H_0 = 0$ and $I \neq 0$) magnetic fields, and under these circumstances, no propagating wave packet is observed.

The nonlinear mode-coupling functions appearing on the right-hand side of Eq. (7) are

$$\begin{aligned}F(n,p) = {} & |n|\Big\{\frac{\chi}{2}\{[1 + \chi(1+(n-p)p)] \\ & + J^2[3 - \chi(n-p)p]\} - B\Big[1 - \frac{p}{2}(3p+n)\Big] \\ & + ip\chi^2 J\Big\},\end{aligned} \tag{9}$$

$$G(n,p) = A|n|[1 - \mathrm{sgn}(np)] - 1, \tag{10}$$

$$\begin{aligned}I(n,p,q) = {} & A|n|[1 - \mathrm{sgn}(nq)] - 1 + |q|\mathrm{sgn}(pq)[|n| \\ & - |n|\mathrm{sgn}(nq) - A],\end{aligned} \tag{11}$$

$$\begin{aligned}\mathcal{J}(n,p,q) = {} & |n|\Big\{\chi\{2J^2(\chi pq - 1) - iq\chi J[1 \\ & + p(n-p-q)]\} + B\Big[1 - 3p^2 \\ & - \frac{3}{2}q(n-p-q)(p^2+1)\Big]\Big\},\end{aligned} \tag{12}$$

and

$$K(n,p,q) = \frac{(A-1)\mathcal{A}(n,p,q)+(A+1)\mathcal{B}(n,p,q)}{2|p|} - \frac{|n|(|p|+A)}{2}. \tag{13}$$

In Eq. (13) we have that

$$\mathcal{A}(n,p,q) = (n-p-q)(2p-p|p|) - \tfrac{1}{2}|p|(|p|-1)(|p|-2), \tag{14}$$

and

$$\mathcal{B}(n,p,q) = (n-p-q)(2p+p|p|) + \tfrac{1}{2}|p|(|p|+1)(|p|+2). \tag{15}$$

In addition, the sgn function equals ± 1 according to the sign of its argument. We stress that Eqs. (7)–(15) are made dimensionless by using the same rescaling utilized to nondimensionalize Eq. (3) in Sec. II A.

Expressions (7)–(15) are the third-order mode-coupling equations describing the time evolution of the interfacial shape of a ferrofluid droplet subjected simultaneously to crossed radial and azimuthal magnetic fields in a Hele-Shaw cell. Note that after neglecting the third-order terms in Eq. (7), and subsequent reintroduction of dimensions, one verifies that Eqs. (7)–(10) agree with the second-order expressions previously derived in Ref. [35]. Our third-order results also reproduce the second-order expressions obtained in earlier studies which analyzed the simplified situation of ferrofluids subjected to purely radial [22,23], or azimuthal [27] magnetic fields in Hele-Shaw geometry. Nevertheless, remember that the inclusion of the third-order terms is essential to a more accurate perturbative description of the shapes and dynamics of the ferrofluid structures under the combined influence of radial and azimuthal applied fields.

III. SHAPE INSTABILITIES IN THE FULLY NONLINEAR REGIME

We initiate our discussion by investigating the impact of two very important governing parameters of the system, namely, the viscosity contrast A, and the ferrofluid's magnetic susceptibility χ, on the dynamic behavior and ultimate shape of the ferrofluid patterns. For the sake of simplicity and clarity, in Figs. 2 and 3, we vary A and χ, while keeping the effective surface tension B unchanged. In this scenario, we adjust the value of the dimensionless current J in such a way that all simulated cases examined in Figs. 2 and 3 have the same real part of the linear growth rate, Eq. (8). By doing this we guarantee that any of the emerging morphological features are associated with nonlinear effects. The influence of B on the patterns will be discussed later in this work.

It is worthwhile to note that, irrespective of their relevance, the interesting results of Ref. [35] have been obtained by considering the specific case in which both A and χ are fixed ($A = -1$ and $\chi = 1$). Therefore, our analysis of Figs. 2 and 3 allows one to explore how the viscosity difference between the ferrofluid and the nonmagnetic fluid (something related to the Saffman-Taylor instability [8–11]), and a key material property of the magnetic fluid sample (i.e., the magnetic susceptibility) affect the morphodynamics of the ferrofluid droplet. Furthermore, from the examination of Figs. 2 and 3 we seek to understand another relevant issue for this pattern-forming system: More precisely, we study the role played by the presence of random perturbations at the initial conditions. By comparing the evolution of initial droplets that are symmetric to those that are random in nature, we examine how the fully nonlinear dynamic stability and ultimate morphology of the simulated ferrofluid shapes are influenced by the inclusion of noise at the early interface.

As commented earlier, we compare late stages of the nonlinear evolution by choosing parameters such that all frames of Figs. 2 and 3 have the same real linear growth rate given by Eq. (8). In this framework, the parameters used for both figures are identical, and the changes between the fingered patterns depicted in Fig. 2 and their counterparts in Fig. 3 are due to differences in their initial conditions. For the patterns displayed in Fig. 2, we impose an initial wavy perturbation with wavenumber $n = n_{\max} = 6$, which is the integer closest to the mode of maximum growth rate, obtained by setting $d\,\mathrm{Re}[\lambda(n)]/dn|_{n=n_{\max}} = 0$. We name these as symmetric initial conditions. On the other hand, in Fig. 3, we consider a superposition of the first 30 modes, each with a random phase. For this reason, such conditions are referred to as random initial conditions. The initial amplitude of all perturbation modes is 10^{-3}. This is small enough so that the patterns undergo linear growth before nonlinear effects become evident. Linear evolution and weakly nonlinear behaviors will be discussed in Sec. IV. We keep the effective surface tension $B = 5.0 \times 10^{-4}$ fixed for all the patterns. In Figs. 2 and 3 the remaining parameters are arranged for three representative values of the viscosity contrast: $A = -0.9$ [(a), (d), and (g)]; $A = 0$ [(b), (e), and (h)]; and, $A = 0.9$ [(c), (f), and (i)]. Notice that for cases in which $A = -0.9$ ($A = 0.9$) the ferrofluid is much more (less) viscous than the nonmagnetic fluid. Of course, when $A = 0$ the ferrofluid and the nonmagnetic fluid have equal viscosities. In addition, for a given A value, we increase the magnetic susceptibility, χ, and tune the dimensionless current J in order to maintain the real part of the linear growth rate [Eq. (8)] unaltered. That gives us $\chi = 0.1$ and $J = 0.69$ [(a), (b), and (c)], $\chi = 0.175$ and $J = 0.90$ [(d), (e), and (f)], $\chi = 0.25$ and $J = 1$ [(g), (h), and (i)].

We begin by analyzing the general behavioral and morphological aspects of the ferrofluid patterns under crossed radial and azimuthal magnetic fields, by inspecting Figs. 2 and 3. Overall, by examining these figures one identifies the development of various types of fingering patterns having six fingers whose specific behaviors and ultimate shapes vary as A, χ, and initial conditions (symmetric in Fig. 2, and random in Fig. 3) are modified. Generally speaking, one can say that, due to the action of the crossed magnetic fields, one verifies the formation of spiky ferrofluid structures (the spikes being induced by the action of the radial magnetic field), presenting skewed fingers which tend to turn in the counterclockwise direction (the turning of the fingers is driven by the coupling between azimuthal and radial magnetic fields). In accordance with what has been previously reported in Ref. [35] for the specific cases in which ($A = -1$ and $\chi = 1$), we have found that all the ferrofluid patterns depicted in Figs. 2 and 3 undergo a rotational motion in the counterclockwise direction. One

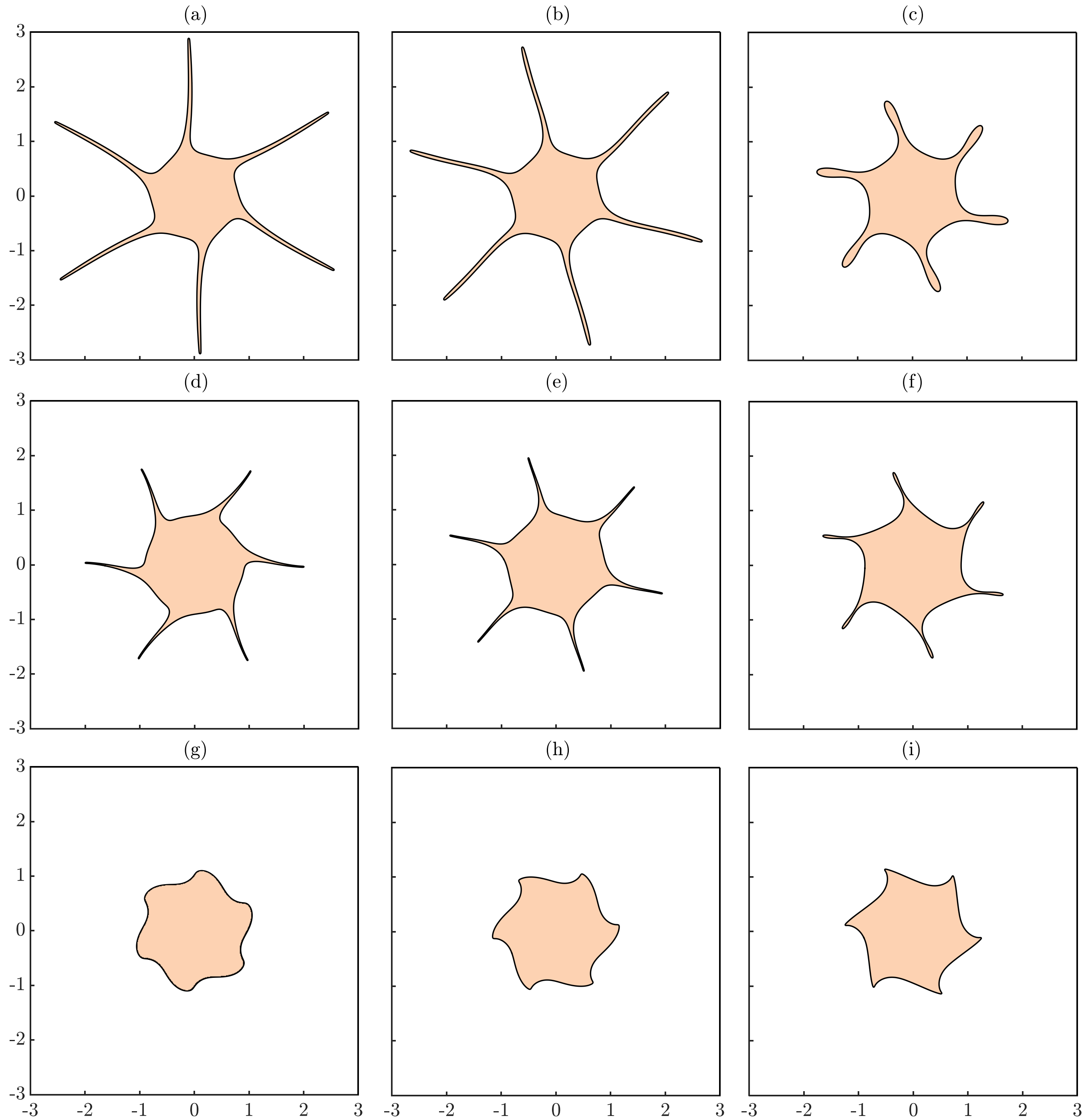

FIG. 2. Representative fully nonlinear patterns for a confined ferrofluid under crossed magnetic fields, generated by using symmetric initial conditions. The patterns are obtained for $A = -0.9$ [(a), (d), and (g)], $A = 0$ [(b), (e), and (h)], and for $A = 0.9$ [(c), (f), and (i)]. In addition, we take $\chi = 0.1$ and $J = 0.69$ [(a)–(c)], $\chi = 0.175$ and $J = 0.90$ [(d)–(f)], and $\chi = 0.25$ and $J = 1$ [(g)–(i)]. The values of the final times taken in these cases are as follows: (a) $t = 29$, (b) $t = 25$, (c) $t = 20.80$, (d) $t = 27.10$, (e) $t = 22.30$, (f) $t = 19.40$, (g) $t = 29$, (h) $t = 25$, and (i) $t = 19.40$. The effective surface tension $B = 5.0 \times 10^{-4}$.

very important result of Ref. [35] was the finding that, for $A = -1$ and $\chi = 1$, the ferrofluid patterns can evolve into stable rotating shapes. In this work, in addition to examining how the morphology of the rotating ferrofluid droplets changes for other values of the governing parameters (including A and χ), under both symmetric and random initial conditions, we also investigate how the stability of the rotating ferrofluid patterns responds to changes in the parameters and consideration of random perturbations.

Prior to examining Figs. 2 and 3, a word of caution: It is important to stress that the shape solution snapshots presented in these figures are *not* necessarily equilibrium states. In fact, as will become clear later in this work, some of the solutions portrayed in Figs. 2 and 3 are steady state, and some

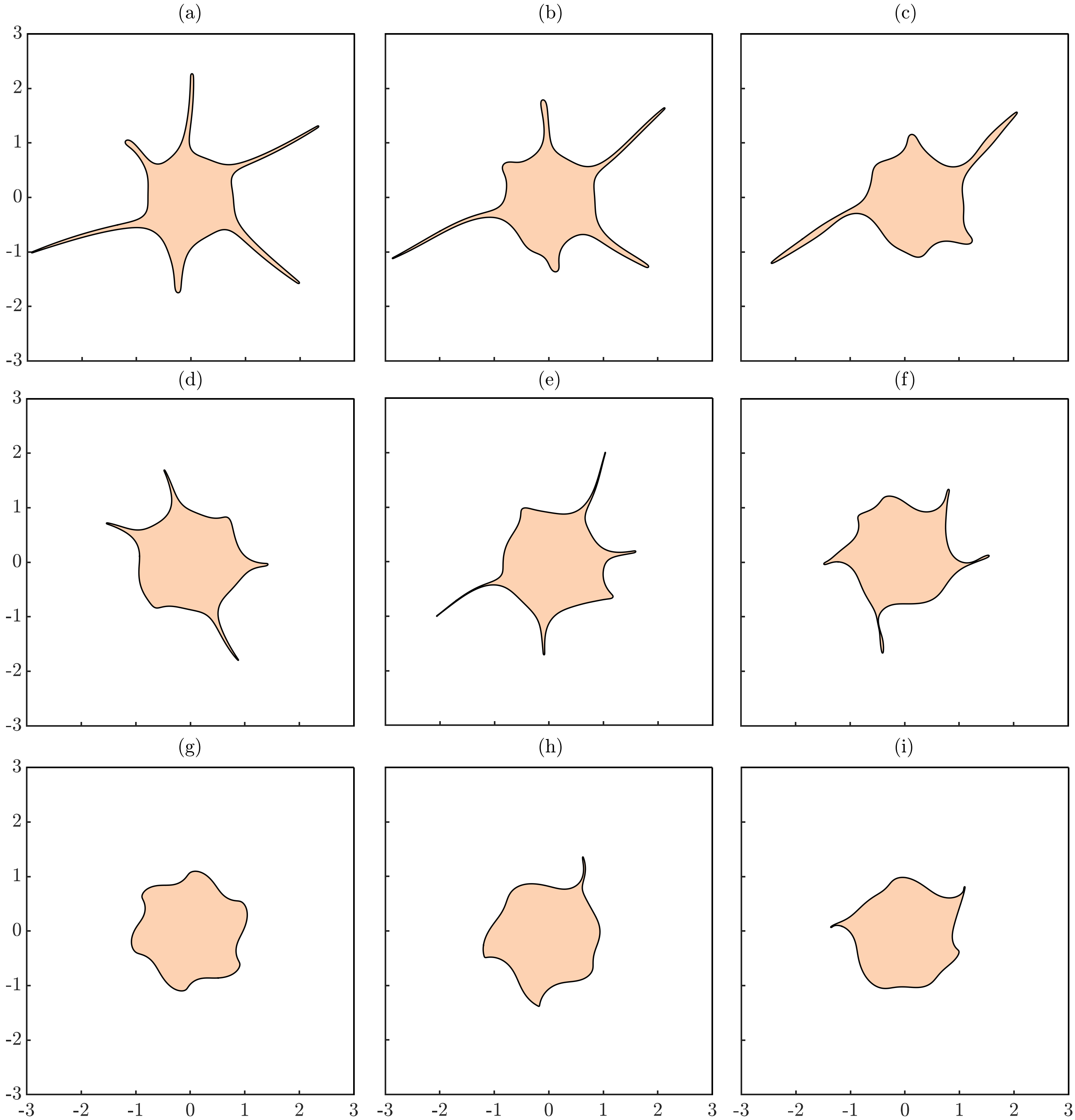

FIG. 3. Representative fully nonlinear patterns for a confined ferrofluid under crossed magnetic fields, generated by using random initial conditions. The patterns are obtained for $A = -0.9$ [(a), (d), and (g)], $A = 0$ [(b), (e), and (h)], and for $A = 0.9$ [(c), (f), and (i)]. In addition, we take $\chi = 0.1$ and $J = 0.69$ [(a)–(c)], $\chi = 0.175$ and $J = 0.90$ [(d)–(f)], and $\chi = 0.25$ and $J = 1$ [(g)–(i)]. The values of the final times taken in these cases are as follows: (a) $t = 25.30$, (b) $t = 21.20$, (c) $t = 17.14$, (d) $t = 24.30$, (e) $t = 19.34$, (f) $t = 15.80$, (g) $t = 60$, (h) $t = 17.56$, and (i) $t = 16.40$. The effective surface tension $B = 5.0 \times 10^{-4}$.

others are transient (i.e., with the fingers continuing to grow indefinitely). These issues are of great importance, and will be thoroughly discussed during the course of this work.

First, we focus on identifying the main morphological aspects of the patterns shown in Fig. 2, for symmetric initial conditions. For a small value of the magnetic susceptibility $\chi = 0.1$ (first row of Fig. 2), and for $A = -0.9$ [Fig. 2(a)] and $A = 0$ [Fig. 2(b)] one verifies the rising of star-shaped patterns having fairly long and thin fingers having pointy tips. In addition, when $A = 0.9$ [Fig. 2(c)] a different structure emerges having shorter, and thicker fingers with bulbous ends. Considering the reduced value of χ, and the fact that in this last case the viscosity contrast is positive (less viscous ferrofluid pushing a more viscous nonmagnetic fluid) one can say that the shape characteristics of the pattern shown in Fig. 2(c) result from the competition of a magnetic and the Saffman-Taylor instability. Another interesting feature clearly revealed in Figs. 2(a)–2(c) is the direction of the fingers of the nonmagnetic fluid penetrating the ferrofluid which depends on the sign of A. For $A = 0.9$ ($A = -0.9$) the invading, inward moving fingers of the nonmagnetic fluid turn to the right (left), while for $A = 0$ the penetrating fingers are more symmetric at their tips, invading the ferrofluid droplet in a more straight manner. These findings indicate that viscous shear effects do play a role in determining the overall shape of the patterns. Similar observations remain valid for the structures illustrated in Figs. 2(d)–2(f) for a larger value of the magnetic susceptibility ($\chi = 0.175$). However, in Figs. 2(g)–2(i), for an even higher value of χ ($\chi = 0.25$) magnetic effects start to dominate, and the viscosity contrast-induced differences among the resulting patterns are not so evident.

At this point, we contrast the patterns generated in Fig. 2 for symmetric initial conditions, with the corresponding ferrofluid structures illustrated in Fig. 3 which have been produced for identical physical parameters, but for random initial conditions. Despite of the visible distinction between the patterns created under symmetric and random conditions, they still share some aspects in common. For instance, all patterns present the same number of fingers. In addition, the fingered structures tend to be long and thin (with sharp tips) for $A \leqslant 0$, and shorter and thicker (with bulbous ends) when $A > 0$. Finally, we have found that all patterns rotate counterclockwise, leading to the formation of skewed ferrofluid fingers that tend to turn in the same direction.

However, the most common element between the patterns in Figs. 2 and 3 is not directly related to their similarity in shape, but refers to their own dynamic stability. As a matter of fact, regardless of whether they are created from symmetric or random conditions, we have found that most of these patterns are indeed unstable. In other words, the majority of these ferrofluid structures will not end up evolving to a stable state in which they rotate indefinitely with an immutable shape.

A convenient way to assess the dynamic instability (or stability) of the rotating ferrofluid patterns under crossed magnetic radial and azimuthal fields is given by the time evolution of the interface perimeter [50–52]. With the application of the crossed magnetic field, the interface deforms, and in the course of time its perimeter starts to grow. If the pattern is dynamically unstable, then its perimeter will keep growing as time progresses. Nevertheless, if the rotating ferrofluid pattern eventually reaches a stable state of permanent profile, its perimeter ceases to vary with time.

By investigating the stability of the rotating ferrofluid patterns via the time evolution of their interfacial perimeters, we have found some interesting results. For instance, we have verified that patterns (d)–(f) in Fig. 2 are unstable. This can be confirmed by examining Fig. 4 which plots the dimensionless interfacial perimeter L as a function of time t, for the ferrofluid patterns portrayed in Figs. 2(d)–2(f) (solid curves), and in Figs. 2(g)–2(i) (dashed curves). For the sake of clarity regarding the unstable nature of the pattern shown in Fig. 2(i) for $A = 0.9$, an extra curve has been added into Fig. 4 for the situation in which $\chi = 0.25$, $J = 1$, and $A = 0.85$ (gray dashed curve).

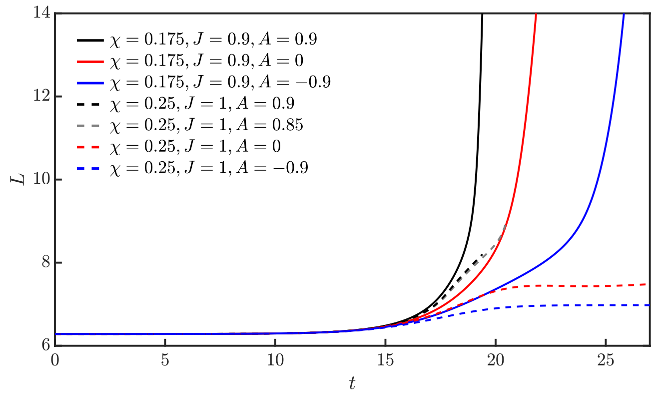

FIG. 4. Time evolution of the interfacial perimeter L for the ferrofluid patterns presented in Figs. 2(d)–2(f) (solid curves) and in Figs. 2(g)–2(i) (dashed curves). Perimeter evolution shows that the nonlinear behavior for $\chi = 0.175$ is unstable regardless the value of the viscosity contrast A. However, stability for $\chi = 0.25$ depends on the value of A, as further described in Fig. 5. The additional gray dashed curve refers to the unstable situation in which $\chi = 0.25$, $J = 1$, and $A = 0.85$.

By following the behavior of the solid curves in Fig. 4, initially one observes a latency time period for which the initially circular ferrofluid shape practically does not change. Then, due to the destabilizing role of the crossed magnetic field one sees a steep growth of L, which keeps growing as time advances. This shows that the patterns appearing in Figs. 2(d)–2(f) are indeed unstable. Incidentally, although not shown in Fig. 4, we have found that this is also the case for the structures disclosed in Figs. 2(a)–2(c). Actually, we have concluded that when a pattern is unstable with a symmetric initial condition, it will be unstable under a random perturbation. However, notice that the opposite is not true. If a pattern turns out to be unstable at late stages having had a random perturbation in the initial condition, the symmetric equivalent may be stable. This is the case of frame (h), which is stable in Fig. 2(h) (as can be explicitly verified in Fig. 4), and unstable in Fig. 3(h). This suggests that in this specific case, we have an instability that is triggered by the random noise. By the way, from these observations, we can say that all patterns (a)–(f) in Figs. 2 and 3 are unstable.

Another curious situation can also be found in the bottom rows of Figs. 2 and 3. The patterns displayed in frames (i) are unstable, for both symmetric and random cases, because of the effect of the viscosity contrast A. This can be seen by examining Fig. 4, since it has a growing perimeter for large t values. As mentioned above, the pattern in Fig. 2(h) is stable, but the equivalent structure in Fig. 3(h) becomes unstable due to the random perturbation. Finally, notice that in Figs. 2(g) and 3(g) the resulting pattern is always stable whether symmetric (as seen in Fig. 4) or random perturbations are imposed as initial conditions. This robust stability behavior, and symmetry recovery (cf. supplemental material) [53] from the random beginnings in Fig. 3(g), appears to be favored by the fact that the system is stable with respect to the Saffman-Taylor instability ($A = -0.9$).

Although not shown, we have also investigated a larger value of the magnetic susceptibility and dimensionless

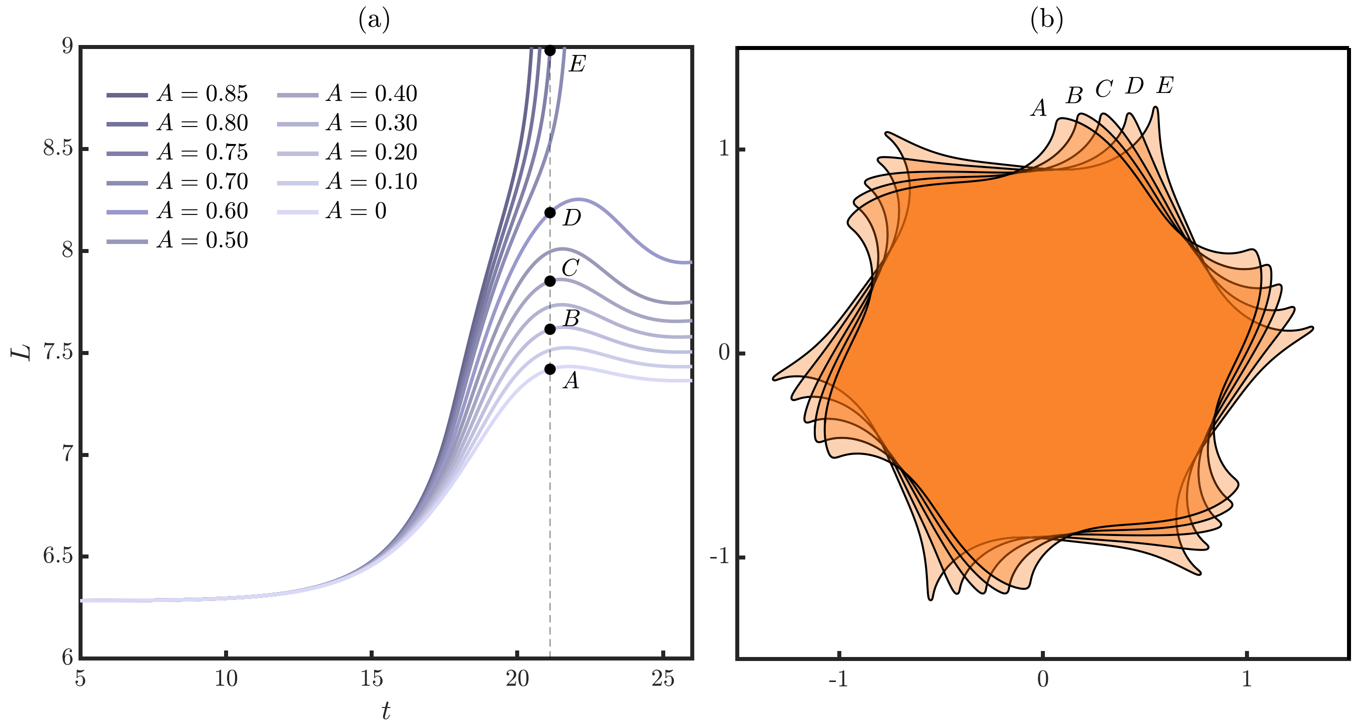

FIG. 5. (a) Perimeter evolution for increasing values of the viscosity contrast, A. The remaining parameters are the same as in Fig. 2 [(g)–(i)], i.e., $B = 5.0 \times 10^{-4}$, $\chi = 0.25$, $J = 1$. The perimeter evolutions for $A \leqslant 0.60$ increase to a maximum and decay, achieving steady state. On the other hand, the perimeter monotonically grows for $A \geqslant 0.70$. A bifurcation point, located in the interval $0.6 \leqslant A \leqslant 0.7$, marks a transition to instability. The dashed line highlights time $t = 21.12$, while the black circles denote the nonlinear shapes superposed in frame (b), for $A = 0, 0.2, 0.4, 0.6$, and 0.75. The phase shift observed in the superposition of the nonlinear shapes result from differences in the rotating speeds, with larger A values having smaller angular velocities, and falling behind in the counterclockwise movement.

current, i.e., $\chi = 0.5$ and $J = 1.12$, which also has the same real linear growth rate as all the parameters investigated in Figs. 2 and 3. We report that the resulting nonlinear shapes for this larger value of χ are very similar to the ones obtained for $\chi = 0.25$ and $J = 1$, displayed in the bottom rows of Figs. 2 and 3. The stability characteristics are also equivalent: For $A = 0.9$ the pattern is unstable with a growing perimeter, and for $A = 0$ and $A = -0.9$ the simulation reaches a steady state and the perimeter saturates. The main difference between the $\chi = 0.25$ and the $\chi = 0.5$ cases is the time in which this steady state is achieved: For the case in which the ferrofluid is more viscous with $A = -0.9$, the saturation time (i.e., $dL/dt|_{t=t_s} = 0$) for the larger χ value is around $t_s = 9$, while $t_s = 22.7$ for $\chi = 0.25$. These observations corroborate the expectation that, for increasing values of the magnetic susceptibility, the magnetic effects are dominant, and differences induced by changes in the viscosity contrast are not so evident in the nonlinear pattern shapes, and manifest mostly in the presence of instability for large A values.

To close the discussion on the influence of the viscosity contrast A, and the magnetic susceptibility χ on the nonlinear interfacial shapes, we briefly deliberate on the counterclockwise angular velocity, and its dependence on these two governing parameters. As already stated, in general, the perturbed initial circular droplet remains unaltered for a while before the skewed radial fingers start to develop. This latency time is clearly shown in the evolution of the perimeter in Fig. 4. During this latency period, the ferrofluid droplet rotates with a constant angular velocity, in agreement with the linear phase velocity, $v(n)$, defined in Sec. II B. As the perimeter grows, we have found that the rotating speeds tend to decrease. In addition, since ferrofluid droplets with larger χ values tend to have smaller perimeters, as indicated by Figs. 2–4, we conclude that larger magnetic susceptibilities are associated with higher rotating speeds.

Now, even though $v(n)$ does not depend on the viscosity contrast, A, we realize that, at the nonlinear level, changes in this parameter also contribute to changes in the angular velocities. This can be recognized by inspecting Fig. 5. For the same parameters as the bottom row of Fig. 2, i.e., $B = 5.0 \times 10^{-4}$, $\chi = 0.25$, $J = 1$, Fig. 5(a) reveals that the perimeter monotonically increases as the viscosity contrast increases. As before, larger perimeters result in reduced angular velocities. This is confirmed by Fig. 5(b), which portrays superposed interfacial patterns that arise at points A, B, C, D, and E, given by the intersection of the vertical dashed line at time $t = 21.12$ in Fig. 5(a). The phase shift observed by the superposition of the nonlinear shapes results from differences in the rotating speeds, with larger A values having smaller angular velocities, and falling behind in the counterclockwise movement.

In addition, one realizes in Fig. 5(a) that the perimeter evolutions for $A \leqslant 0.60$ increase to a maximum and saturate, while for larger A values the nonlinear patterns are unstable and the perimeters grow continuously. This characterizes a bifurcation point for the transition to instability. It is interesting to verify that, in this scenario the own unstable or stable

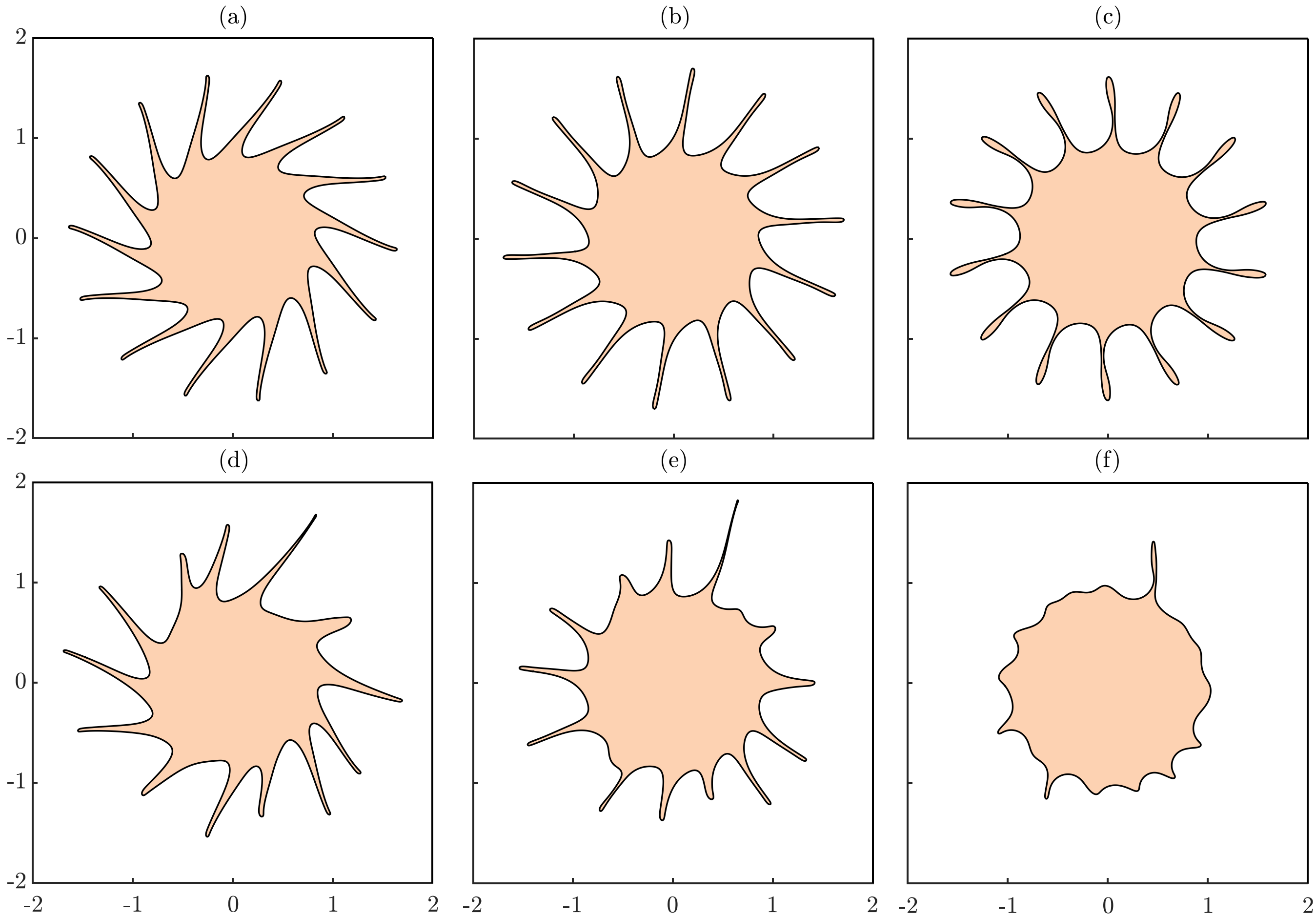

FIG. 6. Fully nonlinear patterns for a confined ferrofluid under crossed magnetic fields, generated by using symmetric [(a)–(c)], and random [(d)–(f)] initial conditions, when $B = 10^{-4}$. The patterns are obtained for $A = -0.9$ [(a) and (d)], $A = 0$ [(b) and (e)], and for $A = 0.9$ [(c) and (f)]. In addition, $\chi = 0.1$ and $J = 0.69$. The values of the final times taken in these cases are: (a) $t = 14.30$, (b) $t = 11.50$, (c) $t = 9.10$, (d) $t = 12$, (e) $t = 8.76$, and (f) $t = 5.20$. All these patterns are unstable.

nature of the rotating ferrofluid shape depends on the value of the viscosity contrast A. Here, only A values larger than 0.6 manage to induce unstable dynamic behavior at late time stages.

To make the parametric study complete, in Fig. 6 we investigate the dynamics for a different value of the effective surface tension parameter B, choosing a smaller value, $B = 10^{-4}$, which has $n_{\max} = 14$ as predicted from linear analysis. We set $A = -0.9$ [Figs. 6(a) and 6(d)]; $A = 0$ [Figs. 6(b) and 6(e)]; and, $A = 0.9$ [Figs. 6(c) and 6(f)]. Moreover, we take $\chi = 0.1$, and $J = 0.69$ as in Fig. 2(a)–2(c). Both symmetric [Figs. 6(a)–6(c)], and random [Figs. 6(d)–6(f)] initial conditions are considered. Figure 6 displays the formation of complex, visually striking ferrofluid patterns. The most emblematic nonlinear features explored in the previous figures of this work are also observed here. We see that the patterns have growing spiky fingers, with the finger directions dependent on A, revealing a tendency towards the formation of bulbous finger tips (and toward fingertip pinch-off) when $A = 0.9$, due to the contribution of the Saffman-Taylor instability. These general nonlinear behaviors for $B = 10^{-4}$ are similar to the cases in which $B = 5.0 \times 10^{-4}$ discussed in Figs. 2–5. This suggests that B does not have a dramatic influence on the fundamental morphological behavior of the patterns, although paramount to determine the number of ramifications.

As a last remark about the results depicted in Figs. 2–9, we ensure that all the dimensionless parameters (A, B, χ, and J) considered in this work are consistent with realistic physical quantities related to existing experiments in confined ferrofluids in Hele-Shaw cell arrangements. For instance, one may consider a ferrofluid droplet of radius $R =$ 1 cm and viscosity $\eta_1 = 2.0 \times 10^{-3}$ Pa s, surrounded by a nonmagnetic fluid of viscosity $10^{-4} \leqslant \eta_2 \leqslant 3.8 \times 10^{-3}$ Pa s. Typically, magnetic susceptibility of ferrofluids varies within $0 < \chi \leqslant 5$, but it can be as high as 40, and surface tension lies in the interval $2.0 \times 10^{-6} \leqslant \sigma \leqslant 6.0 \times 10^{-2}$ N/m. In addition, the radial component of the applied magnetic field varies in the range $0 < H_0 \leqslant 3.2 \times 10^4$ A/m, while the electric current generating the azimuthal field can range from a few mA up until 100 A. By considering dimensional quantities in these intervals, the dimensionless parameters utilized in our work are easily attained. We direct the interested reader to the experimental studies [6,14,20,21,29–32,50,54–63] for a comprehensive review of material properties of ferrofluids and typical physical quantities utilized in laboratories.

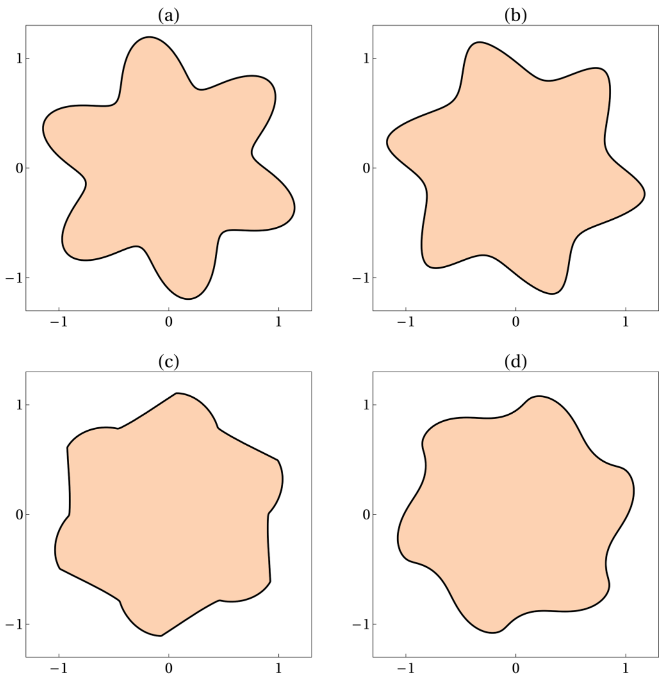

FIG. 7. Comparison of the perturbative solutions for the ferrofluid interface shape obtained by numerically solving Eq. (7) up to (a) first (linear), (b) second, and (c) third order of perturbation, with (d) the fully nonlinear solution found by employing the boundary integral method described in Sec. II A. Here, we set $A = -0.9$, $B = 5 \times 10^{-4}$, $\chi = 0.25$, $J = 1$, and $t = 20$. In addition, the perturbative solutions [(a), (b), and (c)] are plotted by considering the nonlinear coupling of $N = 60$ ($n, 2n, \ldots,$ and $60n$) participating sine and cosine Fourier modes, with $n = n_{\max} = 6$ being the fundamental mode.

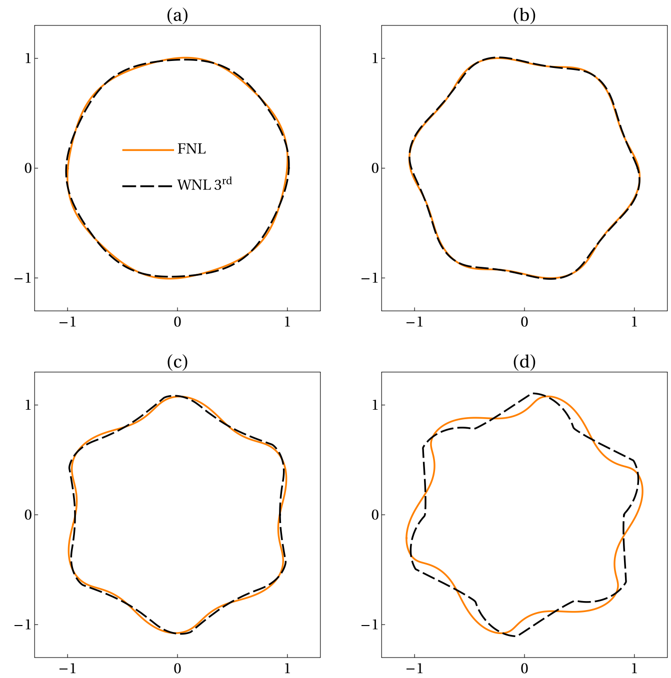

FIG. 8. Snapshots illustrating the time evolution of the ferrofluid interface as predicted by the third-order WNL solution (dashed curves), superposed to the corresponding FNL shape (solid curves). The values of time taken in each frame are (a) $t = 10$, (b) $t = 15$, (c) $t = 17$, and (d) $t = 20$. The other physical parameters and initial conditions used here are identical to those utilized in Fig. 7.

IV. PERTURBATIVE VS FULLY NONLINEAR SHAPES

In Sec. III, we have found a variety of pattern-forming structures and dynamical responses of the ferrofluid interface as the relevant dimensionless parameters of the system A, B, χ, and J were varied. Most of the produced fully nonlinear patterns exhibit considerable intricate shapes, presenting the formation of long fingered structures. Of course, these kinds of interfacial behaviors can only be appropriately described by fully nonlinear computational methods such as the boundary integral scheme employed in this work. Nevertheless, by closer inspection of the patterned structures depicted in Fig. 2, we note that in some cases, the magnetically induced viscous fingering patterns are not so excessively disturbed. More specifically, the less deformed structures illustrated in Figs. 2(g)–2(i) develop short skewed fingers with lengths notably smaller than the unperturbed radius R of the ferrofluid droplet. Although these patterns are formed in the fully nonlinear (FNL) regime of the dynamics, it seems that a perturbative weakly nonlinear (WNL) approach could access these shape instabilities, given that their amplitudes are small.

In this section, we investigate how some perturbative solutions obtained from the mode-coupling Eq. (7) compare to an equivalent fully nonlinear shape obtained by using boundary integral simulations. We do this by systematically increasing the perturbation order from first (purely linear) up to third order. By doing this, we aim to extract the most important morphological features of the emerging ferrofluid patterns, and possibly get perturbative pattern-forming structures that progressively resemble the symmetric, and less deformed fully nonlinear shapes, as those portrayed in Figs. 2(g)–2(i).

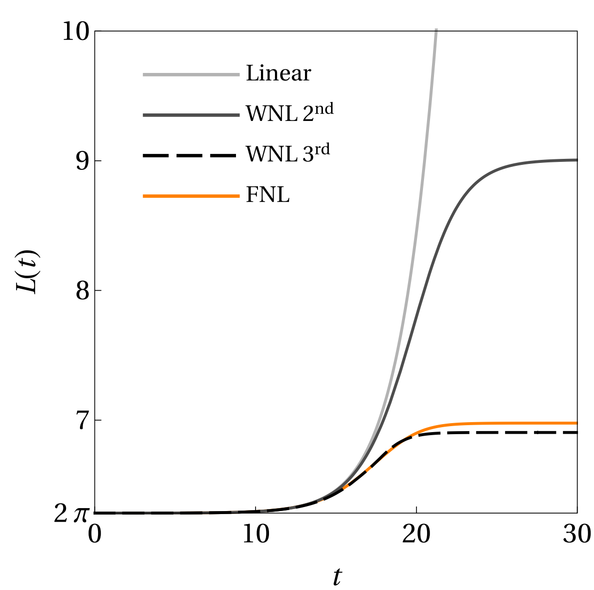

FIG. 9. Behavior of the interfacial perimeter $L(t)$ with respect to variations in time t, corresponding to the situations leading to the patterns illustrated in Fig. 7. All physical parameters and initial conditions used here are identical to those utilized in Fig. 7.

To illustrate how perturbative solutions approach the corresponding long-time simulated structures, we pick the simplest fully nonlinear ferrofluid pattern depicted in Fig. 2, namely Fig. 2(g), as a base for comparison. In this way, in Fig. 7 we plot the ferrofluid droplet shapes obtained by utilizing the perturbative solutions of the mode-coupling Eq. (7) up to first [Fig. 7(a)], second [Fig. 7(b)], and third [Fig. 7(c)] order of perturbation, plus the equivalent fully nonlinear pattern [Fig. 7(d)]. As in Fig. 2(g), all ferrofluid patterns depicted in Fig. 7 are obtained by considering the parameters $A = -0.9$, $B = 5 \times 10^{-4}$, $\chi = 0.25$, and $J = 1$. Moreover, the snapshots displayed in Fig. 7 are taken at time $t = 20$.

Before proceeding with the analysis of Fig. 7, we briefly explain how the perturbative solutions of the first (linear), second (WNL second), and third orders (WNL third) are plotted. First, we consider the nonlinear coupling of $N = 60$ Fourier modes, namely the fundamental mode $n = n_{\max} = 6$ and its harmonics $2n, 3n, \ldots,$ and $60n$, and rewrite the net interfacial perturbation $\zeta(\varphi, t)$ in terms of the real-valued cosine $a_n(t) = \zeta_n(t) + \zeta_{-n}(t)$, and sine $b_n(t) = i[\zeta_n(t) - \zeta_{-n}(t)]$ amplitudes. The time evolution of the mode amplitudes $a_n(t)$ and $b_n(t)$ can then be obtained by numerically solving the corresponding coupled nonlinear differential equations. Of course, the time evolution of these amplitudes depend on the order of perturbation that is being considered in Eq. (7). Once this is done, the shape of the evolving interface can be easily acquired by utilizing

$$\begin{aligned}\mathcal{R}(\varphi, t) = 1 + \zeta_0 + [a_n(t)\cos(n\varphi) + a_{2n}(t)\cos(2n\varphi) + \cdots \\ + a_{60n}(t)\cos(60n\varphi)] + [b_n(t)\sin(n\varphi) \\ + b_{2n}(t)\sin(2n\varphi) + \cdots + b_{60n}(t)\sin(60n\varphi)],\end{aligned} \tag{16}$$

where ζ_0 is an intrinsically nonlinear constraint related to the ferrofluid droplet mass conservation, as indicated at the beginning of Sec. II B.

Based on the symmetry properties of the fully nonlinear structure [Fig. 7(d)], and without loss of generality, we set the initial ($t = 0$) harmonic mode amplitudes to zero, i.e., $a_{2n}(0) = a_{3n}(0) = \ldots = a_{Nn}(0) = 0$, and $b_{2n}(0) = b_{3n}(0) = \ldots = b_{Nn}(0) = 0$, where $N = 60$. Therefore, at $t = 0$ only the fundamental cosine mode n has a nonzero amplitude $|a_n(0)| = 10^{-3}$, and $b_n(0) = 0$. This guarantees that the interfacial behaviors we detect are spontaneously generated by the weakly nonlinear dynamics, and not by artificially imposing large initial amplitudes for the harmonic modes. Note that the fully nonlinear pattern depicted in Fig. 7(d) has also been obtained under these same initial conditions.

We initiate our discussion by examining Figs. 7(a) and 7(d), which depict the ferrofluid patterns generated by utilizing the linear perturbative solution, and its fully nonlinear counterpart, respectively. By contrasting the linear interfacial shape in Fig. 7(a) with the FNL pattern in Fig. 7(d), it is evident that the first-order perturbative solution does not accurately match the FNL ferrofluid structure. Note that the six smooth protuberances emerging at the ferrofluid boundary in Fig. 7(a) have considerably larger amplitudes than the FNL instabilities presented in Fig. 7(d). Furthermore, the purely linear, sinusoidal fingered structures do not resemble the short counterclockwise skewed fingers appearing in the FNL pattern. Recall that in the first-order perturbative description of the dynamics, the Fourier modes decouple, and the pattern illustrated in Fig. 7(a) is a consequence of the exponential growth of a single mode, namely the fundamental mode $n = n_{\max} = 6$. Therefore, it is reasonably expected that this simple, lowest perturbative order solution cannot capture the more intricate features of a FNL interface shape.

Motivated by the poor agreement between the linear perturbative pattern, and the FNL shape, we increase the complexity of our perturbative solution by considering one more order of perturbation, extending our linear perturbative description to a WNL second-order solution. The resulting WNL second-order perturbative pattern is presented in Fig. 7(b). The most noteworthy feature revealed by this second-order perturbative shape is the presence of slightly bent fingers which are sharper at their tips than the corresponding fingered shapes obtained in Fig. 7(a). These aspects make the WNL second-order structure a bit more similar to the FNL pattern found in Fig. 7(d). This more structured second-order morphology arises due to the growth and interaction of various participating modes, other than just the dominant fundamental mode, as in Fig. 7(a) for the linear interface. The nonlinear coupling between Fourier modes tend to make the fingers sharper, and also act to restrain the purely exponential growth that occurred at the linear level. Therefore, one can say that the inclusion of an extra order in the perturbative description of the problem has a positive impact on the morphology of the resulting pattern. Nevertheless, the lengths of the fingers, and the overall aspect of the second-order pattern shown in Fig. 7(b) are still in discordance with the corresponding features of the FNL structure displayed in Fig. 7(d). So, despite the morphological improvements provided by the WNL second-order solution, it is clear that this description is still not good enough to properly describe the actual ferrofluid droplet shape, and that an extra order of perturbation must be included.

We continue by extending our perturbative description up to third-order, and use it to generate the weakly nonlinear pattern shown in Fig. 7(c). When compared with the structures discussed previously in Figs. 7(a) and 7(b), the differences are quite evident. It is apparent that the WNL third-order pattern disclosed in Fig. 7(c) does present the most important morphological characteristics of the FNL shape illustrated in Fig. 7(d). By inspecting Fig. 7(c), one can verify the formation of a pattern presenting short-length fingers which are skewed in the counterclockwise direction, similar to the FNL shape portrayed in Fig. 7(d). Aside from the straight edges and peaky fingertips appearing in the perturbative interfacial shape, one may say that the structures shown in Figs. 7(c) and 7(d) share a close resemblance. Incidentally, such small differences between the WNL third-order solution and its FNL counterpart are expected due to the intrinsic limitations of a truncated perturbative scheme. However, it is reassuring to see the the WNL third-order solution does a good job in reproducing the actual FNL shape. These mode-coupling results demonstrate that our willingness to go to such a high-order perturbation level has been rewarded by the emergence of a pattern-forming structure closely related to the more elaborate FNL shape obtained by using boundary integral numerical simulations.

Although in Fig. 7 we have demonstrated a good morphological agreement between the WNL third-order solution and the corresponding FNL pattern, it is still of relevance to investigate the dynamics prior to the establishment of the patterns portrayed in Figs. 7(c) and 7(d) for $t = 20$, at intermediate values of time ($t \leqslant 20$). This relevant matter is addressed in Fig. 8, where we plot snapshots of the interface illustrating the time evolution of the ferrofluid droplet shape as predicted by the WNL third-order solution (dashed curves), superposed to the corresponding FNL pattern (solid curves). These representative snapshots are obtained at times (a) $t = 10$, (b) $t = 15$, (c) $t = 17$, and (d) $t = 20$. By contrasting the WNL third-order patterns depicted in frames (a), (b), and (c) to the corresponding FNL interfacial shapes, one verifies that the perturbative approach indeed offers an excellent approximation to the interfacial shape obtained by numerical means, since the difference between the interfacial morphologies predicted by these two different methods is very small. As time increases and the fingers develop further, one perceives a more noticeable difference between the morphologies, as shown in frame (d). In addition, note that in Fig. 8(d), the perturbative shape is slightly out of phase when compared to the numerical pattern, indicating that the WNL pattern rotates with a different speed than the corresponding FNL interface.

By scrutinizing Eqs. (7)–(15) it is clear that the third-order terms add extra complexity to the description of the problem. However, the inclusion of these terms are necessary to provide a more thorough description of the interface dynamics than previous first- and second-order approaches [22,23,35]. Note that contributions coming from higher perturbative orders [e.g., $O(\zeta_n^4)$, $O(\zeta_n^5)$, etc.] are less important than the first, second, and third orders, due to the smallness of ζ_n with respect to R ($|\zeta_n| \ll R$). Nevertheless, these contributions can still provide a noticeable improvement in the morphological agreement between WNL perturbative solutions and FNL shapes. On the other hand, the consideration of perturbative terms beyond the third-order is not trivial to implement, and would make the mode-coupling equation simply humongous and very cluttered.

To further validate the conclusions reached from the analysis of Figs. 7 and 8 in a more quantitative fashion, in Fig. 9 we plot the time evolution of the dimensionless perimeter $L(t)$ of the interfaces associated to each situation examined in Fig. 7. Note that, for the perturbative solutions, the time-dependent interfacial perimeter is given by

$$L(t) = \int_0^{2\pi} \sqrt{\mathcal{R}^2(t) + \left[\frac{d\mathcal{R}(t)}{d\varphi}\right]^2}\, d\varphi. \tag{17}$$

Inspecting the four curves in Fig. 9, we note that initially all of them overlap. First, one observes a latency time period for which the perimeter does not change, indicating that the interface remains circular. Then, due to the destabilizing action of the applied magnetic field, the ferrofluid droplet starts to deform. At this early stage of the dynamics, the perturbations emerging at the fluid-fluid boundary are very small, and nonlinear effects are negligible. Therefore, the nonlinear curves (WNL and FNL) coincide with the linear one.

Nonetheless, as time advances and nonlinear effects start to become important, each nonlinear curve in Fig. 9 reaches a maximum value, and saturates, while the linear curve continues to grow exponentially. This is consistent with the fact that the linear perturbative description fails to predict the proper dynamical behavior of the interface for larger values of time. Conversely, both WNL curves capture the saturation of the perimeter occurring at longer time values. However, while the WNL second-order curve saturates at $L(t) \approx 9.00$, the WNL third-order curve reaches its maximum at $L(t) \approx 6.90$. This WNL third-order value is indeed much closer to the perimeter $L(t) \approx 6.98$ attained by the FNL curve, when a stable rotating droplet shape is detected. Furthermore, notice that the time t_s for which saturation occurs is considerably overestimated by the WNL second-order curve ($t_s \approx 28.5$) when compared with the corresponding times $t_s \approx 22.0$, and $t_s \approx 22.7$ obtained by the WNL third-order, and FNL solutions, respectively.

The findings presented in Figs. 7–9 point to the fact that the employment of a third-order perturbative description of the problem is not only necessary to provide a better morphological agreement between perturbative patterns and fully nonlinear shapes, but also needed to accurately predict the development of fully nonlinear, spinning ferrofluid droplets that evolve into stable interfacial profiles as detected in Ref. [35] and also in Sec. III of this work.

Finally, it should be stressed that, as long as the ferrofluid patterns are not too deformed, the important dynamic behaviors identified in Figs. 7–9 are indeed quite general and representative of what occurs when similar comparisons of linear and WNL solutions are performed with corresponding FNL results when other values of the governing parameters A, B, χ, and J are used.

V. CONCLUDING REMARKS

It is well known in the ferrohydrodynamic literature that the employment of different applied magnetic field configurations results in a great variety of dynamic responses and morphological behaviors for ferrofluid droplets confined in Hele-Shaw cells. An interesting, recent theoretical study on this topic [35] has revealed a particularly attractive aspect of the problem: The use of crossed radial and azimuthal magnetic fields leads to the formation of peculiar swirling ferrofluid patterns having skewed fingers, which rotate with a controllable angular velocity, with stable permanent interfacial profiles. In Ref. [35], this appealing pattern-forming behavior has been examined by focusing on particular parametric circumstances, in which the viscosity contrast $A = -1$ (i.e., viscous ferrofluid droplet surrounded by a nonmagnetic fluid of negligible viscosity), and for a relatively large value of the ferrofluid magnetic susceptibility $\chi = 1$.

In this work, we revisited the problem of a confined ferrofluid droplet under the influence of crossed radial and azimuthal magnetic fields, and examined still unexplored facets of its rich pattern formation dynamics. Boundary integral numerical simulations, and a third-order perturbative mode-coupling scheme were employed to reveal how the morphology of the rotating ferrofluid droplets, and their dynamic instability respond to changes in the dimensionless governing parameters of the system, namely: The viscosity contrast A, the ferrofluid's magnetic susceptibility χ, the effective surface tension B (ratio of capillary to magnetic forces), and the current parameter J (relative magnitude of azimuthal and radial fields). By conveniently tuning J to keep the same linear growth for all situations, and by keeping B fixed, we have been able to unveil, by varying A and χ, a gallery of various possible shapes for the rotating ferrofluid droplet, ranging from starlike patterns having long thin fingers with sharp tips, or structures with thicker and shorter fingers having bulbous ends, through distorted polygonal-like shapes having skewed fingers at their vertices.

Fundamentally, these families of shapes result from the competition between magnetic and viscous fingering instabilities. We also verified that smaller values of B lead to more deformed patterns having a larger number of emerging fingers. Still regarding the morphological aspects of the patterns, we compared numerically simulated fully nonlinear shapes with equivalent perturbative structures for increasing perturbation orders (first, second, and third). We found that the inclusion of third-order mode-coupling contributions is necessary to provide a more accurate agreement between fully nonlinear and perturbative solutions for the interface shapes.

Further development of this work is connected with accounting for the role played by the system's governing dimensionless parameters on the dynamic instability of the spinning ferrofluid droplets. Our numerical simulations revealed that modifications of the governing parameters may have a nontrivial impact on the stability of the patterns. We concluded that, despite having the same initial linear growth, nonlinear patterns predicted as stable for a given set of controlling parameters (A, χ B, and J) can become dynamically unstable if some of these parameters are changed. In particular, as the viscosity contrast, A, is increased and the ferrofluid droplet becomes less viscous than then outer nonmagnetic fluid, a viscous instability contributes to the magnetically driven fingering growth. Interestingly, for particular cases in which the calculated shapes are stable (e.g., $\chi = 0.25$, $B = 5 \times 10^{-4}$, and $J = 1$), the patterns only become unstable for $A > 0.6$.

In addition, we investigated how the shape and dynamic stability of the patterns are affected by initial conditions. This was done by contrasting the pattern-forming structures rising by imposing symmetric and random initial conditions. The imposition of random initial conditions is a convenient way to test the robustness of the stable dynamic nature of a given pattern. In that sense, we have found patterns presenting stable shapes (e.g., $A = 0$, $\chi = 0.25$, $B = 5 \times 10^{-4}$, and $J = 1$) when a symmetric initial condition is imposed that turned out unstable under random perturbations. In general, by contrasting a number of patterns, under symmetric and random conditions, and for various parametric situations, we have found that for $0 \leqslant \chi \leqslant 0.5$ and $-0.9 \leqslant A \leqslant 0.9$, most of the structures are indeed dynamically unstable. Our results indicate that dynamic stability of the rotating ferrofluid patterns under radial and azimuthal crossed magnetic fields is favored for larger, negative values of the viscosity contrast A ($A \to -1$), and values of the ferrofluid's magnetic susceptibility greater than $\chi \geqslant 0.25$. This is in accordance with the findings of Ref. [35] that explored the parameter regime $A = -1$ and $\chi = 1$.

ACKNOWLEDGMENTS

R.M.O. and J.A.M. thank CNPq (Conselho Nacional de Desenvolvimento Científico e Tecnológico) for financial support under Grants No. 434347/2018-3 and No. 305140/2019-1, respectively.

[1] R. E. Rosensweig, *Ferrohydrodynamics* (Cambridge University Press, Cambridge, UK, 1985).

[2] E. Blums, A. Cebers, and M. M. Maiorov, *Magnetic Fluids* (de Gruyter, New York, 1997).

[3] J.-C. Bacri, R. Perzynski, and D. Salin, Magnetic liquids, Endeavour **12**, 76 (1988).

[4] C. Rinaldi, A. Chaves, S. Elborai, X. He, and M. Zahn, Magnetic fluid rheology and flows, Curr. Opin. Colloid Interface Sci. **10**, 141 (2005).

[5] D. Andelman and R. E. Rosensweig, Modulated phases: Review and recent results, J. Phys. Chem. B **113**, 3785 (2009).

[6] A. Zakinyan, E. Beketova1, and Y. Dikansky, Flows and instabilities of ferrofluids at the microscale, Microfluid Nanofluid **21**, 88 (2017).

[7] S. Afkhami and Y. Renardy, Ferrofluids and magnetically guided superparamagnetic particles in flows: A review of simulations and modeling, J. Eng. Math. **107**, 231 (2017).

[8] G. M. Homsy, Viscous fingering in porous media, Annu. Rev. Fluid Mech. **19**, 271 (1987).

[9] K. V. McCloud and J. V. Maher, Experimental perturbations to Saffman-Taylor flow, Phys. Rep. **260**, 139 (1995).

[10] P. G. Saffman and G. I. Taylor, The penetration of a fluid into a porous medium or Hele-Shaw cell containing a more viscous liquid, Proc. R. Soc. Lond. A **245**, 312 (1958).

[11] J. A. Miranda and M. Widom, Radial fingering in a Hele-Shaw cell: A weakly nonlinear analysis, Physica D **120**, 315 (1998).

[12] A. O. Tsebers and M. M. Maiorov, Magnetostatic instabilities in plane layers of magnetizable liquids, Magnetohydrodynamics (NY) **16**, 21 (1980).

[13] A. O. Tsebers, Dynamics of magnetostatic instabilities, Magnetohydrodynamics (NY) **17**, 113 (1981).

[14] D. P. Jackson, R. E. Goldstein, and A. O. Cebers, Hydrodynamics of fingering instabilities in dipolar fluids, Phys. Rev. E **50**, 298 (1994).

[15] J. Kent-Dobias and A. J. Bernoff, Energy-driven pattern formation in planar dipole-dipole systems in the presence of weak noise, Phys. Rev. E **91**, 032919 (2015).

[16] P. B. Canham, The minimal energy of bending as a possible explanation of the bioconcave shape of the human red blood cell, J. Theor. Biol. **26**, 61 (1970).

[17] T. H. Bergeman, G. Erez, and H. J. Metcalf, Magnetostatic trapping field for neutral atoms, Phys. Rev. A **35**, 1535 (1987).

[18] J. G. E. Harris, R. A. Michniak, S. V. Nguyen, W. C. Campbell, D. Egorov, S. E. Maxwell, L. D. van Buuren, and J. M. Doyle, Deep superconducting magnetic traps for neutral atoms and molecules, Rev. Sci. Instrum. **75**, 17 (2004).

[19] T. P. Meyrath, Experiments with Bose-Einstein condensation in an optical box, Ph.D. thesis, The University of Texas at Austin, 2005.

[20] C.-Y. Chen, Y.-S. Yang, and J. A. Miranda, Miscible ferrofluid patterns in a radial magnetic field, Phys. Rev. E **80**, 016314 (2009).

[21] C.-Y. Chen, W.-L. Wu, and J. A. Miranda, Magnetically induced spreading and pattern selection in thin ferrofluid drops, Phys. Rev. E **82**, 056321 (2010).

[22] R. M. Oliveira, J. A. Miranda, and E. S. G. Leandro, Ferrofluid patterns in a radial magnetic field: Linear stability, nonlinear dynamics, and exact solutions, Phys. Rev. E **77**, 016304 (2008).

[23] P. H. A. Anjos, S. A. Lira, and J. A. Miranda, Fingering patterns in magnetic fluids: Perturbative solutions and the stability of exact stationary shapes, Phys. Rev. Fluids **3**, 044002 (2018).

[24] R. M. Oliveira and J. A. Miranda, Fully nonlinear simulations of ferrofluid patterns in a radial magnetic field, Phys. Rev. Fluids **5**, 124003 (2020).

[25] J. A. Miranda, Rotating Hele-Shaw cells with ferrofluids, Phys. Rev. E **62**, 2985 (2000).

[26] D. P. Jackson and J. A. Miranda, Controlling fingering instabilities in rotating ferrofluids, Phys. Rev. E **67**, 017301 (2003).

[27] E. O. Dias and J. A. Miranda, Azimuthal field instability in a confined ferrofluid, Phys. Rev. E **91**, 023020 (2015).

[28] C.-Y. Chen and T.-S. Lin, in *Advances in Computational Fluid-Structure Interaction and Flow Simulation*, edited by Y. Bazilevs and K. Takizawa (Springer Nature, Basel, 2016).

[29] C. Lorenz and M. Zahn, Hele-Shaw ferrohydrodynamics for rotating and DC axial magnetic fields, Phys. Fluids Gallery Fluid Motion **15** (9), S4 (2003).

[30] S. Rhodes, J. Perez, S. Elborai, S.-H Lee, and M. Zahn, Ferrofluid spiral formations and continuous-to-discrete phase transitions under simultaneously applied DC axial and AC in-plane rotating magnetic Fields, J. Magn. Magn. Mater. **289**, 353 (2005).

[31] S. Elborai, D.-K. Kim, X. He, S.-H Lee, S. Rhodes, and M. Zahn, Self-forming, quasi-two-dimensional, magnetic-fluid patterns with applied in-plane-rotating and dc-axial magnetic fields, J. Appl. Phys. **97**, 10Q303 (2005).

[32] S. Rhodes, X. He, S. Elborai, S.-H. Lee, and M. Zahn, Magnetic fluid behavior in uniform DC, AC, and rotating magnetic Fields, J. Electrostat. **64**, 513 (2006).

[33] D. P. Jackson and J. A. Miranda, Confined ferrofluid droplet in crossed magnetic fields, Eur. Phys. J. E **23**, 389 (2007).

[34] C.-Y. Chen, S.-Y. Wu, and J. A. Miranda, Fingering patterns in the lifting flow of a confined miscible ferrofluid, Phys. Rev. E **75**, 036310 (2007).

[35] Z. Yu and I. C. Christov, Tuning a magnetic field to generate spinning ferrofluid droplets with controllable speed via nonlinear periodic interfacial waves, Phys. Rev. E **103**, 013103 (2021).

[36] O. Sandre, C. Ménager, J. Prost, V. Cabuil, J.-C. Bacri, and A. Cebers, Shape transitions of giant liposomes induced by an anisotropic spontaneous curvature, Phys. Rev. E **62**, 3865 (2000).

[37] G. Z. Lum, Z. Ye, X. Dong, H. Marvi, O. Erin, W. Hu, and M. Sitti, Shape-programmable magnetic soft matter, Proc. Natl. Acad. Sci. USA **113**, E6007 (2016).

[38] T. Xu, J. Zhang, M. Salehizadeh, O. Onaizah, and E. Diller, Millimeter-scale flexible robots with programmable three-dimensional magnetization and motions, Sci. Rob. **4**, eaav4494 (2019).

[39] J. Giltinan, P. Katsamba, W. Wang, E. Lauga, and M. Sitti, Selectively controlled magnetic microrobots with opposing helices, Appl. Phys. Lett. **116**, 134101 (2020).

[40] F. Serwane, A. Mongera, P. Rowghanian, D. A. Kealhofer, A. A. Lucio, Z. M. Hockenbery, and O. Campàs, In vivo quantification of spatially-varying mechanical properties in developing tissues, Nat. Methods **14**, 181 (2017).

[41] C. Wilhelm, F. Gazeau, and J.-C. Bacri, Magnetic micromanipulation in the living cell, Europhys. News **36**, 89 (2005).

[42] B. J. Nelson, I. K. Kaliakatsos, and J. J. Abbott, Microrobots for minimally invasive medicine, Annu. Rev. Biomed. Eng. **12**, 55 (2010).

[43] G. Tryggvason and H. Aref, Numerical experiments on Hele-Shaw flow with a sharp interface, J. Fluid Mech. **136**, 1 (1983).

[44] G. Birkhoff, Taylor instability and laminar mixing, Los Alamos Scientific Laboratory Technical Report No. LA-1862, pp. 1–76, 1954 (unpublished). See also, G. Birkhoff, Taylor instability: appendices to Report LA-1862, Los Alamos Scientific Laboratory Technical Report No. LA-1927, pp. 1–91, 1956 (unpublished).

[45] W.-S. Dai and M. J. Shelley, A numerical study of the effect of surface tension and noise on an expanding Hele-Shaw bubble, Phys. Fluids A **5**, 2131 (1993).

[46] T. Y. Hou, J. S. Lowengrub, and M. J. Shelley, Boundary integral methods for multicomponent fluids and multiphase materials, J. Comput. Phys. **169**, 302 (2001).

[47] T. Y. Hou, J. S. Lowengrub, and M. J. Shelley, Removing the stiffness from interfacial flows with surface tension, J. Comput. Phys. **114**, 312 (1994).

[48] H. D. Ceniceros, T. Y. Hou, and H. Si, Numerical study of Hele-Shaw flow with suction, Phys. Fluids **11**, 9 (1999).

[49] M. Igonin, Hydrodynamic instabilities of miscible and immiscible magnetic fluids in a Hele-Shaw cell, Ph.D. thesis, D. Diderot University Paris 7, 2004.

[50] S. Langer, R. E. Goldstein, and D. P. Jackson, Dynamics of labyrinthine pattern formation in magnetic fluids, Phys. Rev. A **46**, 4894 (1992).

[51] M. J. Shelley, F.-R. Tian, and K. Wlodarski, Hele-Shaw flow and pattern formation in a time-dependent gap, Nonlinearity **10**, 1471 (1997).

[52] C.-Y. Chen, C.-H. Chen, and J. A. Miranda, Numerical study of miscible fingering in a time-dependent gap Hele-Shaw cell, Phys. Rev. E **71**, 056304 (2005).

[53] See Supplemental Material at http://link.aps.org/supplemental/10.1103/PhysRevE.104.065113 for a video of this process.

[54] J.-C. Bacri and D. Salin, First-order transition in the instability of a magnetic fluid interface, J. Phys. Lett. **45**, 559 (1984).

[55] C. Flament, G. Pacitto, J. C. Bacri, I. Drikis, and A. Cebers, Viscous fingering in a magnetic fluid. I. Radial Hele-Shaw flow, Phys. Fluids **10**, 2464 (1998).

[56] N. J. Hillier and D. P. Jackson, Width of a ferrofluid finger: Hysteresis and a double energy minimum, Phys. Rev. E **75**, 036314 (2007).

[57] A. J. Dickstein, S. Erramilli, R. E. Goldstein, D. P. Jackson, and S. A. Langer, Labyrinthine pattern formation in magnetic fluids, Science **261**, 1012 (1993).

[58] G. Pacitto, C. Flament, J. C. Bacri, and M. Widom, Rayleigh-Taylor instability with magnetic fluids: Experiment and theory, Phys. Rev. E **62**, 7941 (2000).

[59] G. Pacitto, C. Flament, and J. C. Bacri, Viscous fingering in a magnetic fluid. II. Linear Hele-Shaw flow, Phys. Fluids **13**, 3196 (2001).

[60] C.-Y. Chen, W.-K. Tsai, and J. A. Miranda, Hybrid ferrohydrodynamic instability: Coexisting Peak and labyrinthine patterns, Phys. Rev. E **77**, 056306 (2008).

[61] H. Li, C. Y. Kao, and C.-Y. Wen, Labyrinthine and secondary wave instabilities of a miscible magnetic fluid drop in a Hele-Shaw cell, J. Fluid Mech. **836**, 374 (2018).

[62] W. H. Liao and D. A. Krueger, Theory of large agglomerates in magnetic colloids, J. Colloid Interface Sci. **70**, 564 (1979).

[63] C. Flament, S. Lacis, A. Cebers, S. Neveu, and R. Perzynski, Measurements of ferrofluid surface tension in confined geometry, Phys. Rev. E **53**, 4801 (1996).